What Gear Ratio Makes QDD Actuators Robust Against Impacts? A Theoretical Limit and Interactive Tool for Legged Robots

Anton Shu[1,2], Konrad Fruend[1], Fabian Beck[1], Tristan Ehlert[1], Alexander Kolb[1], Natalija Topalovic[1], Clara Raschel[1], Sebastian Wolf[1], Marco Hutter[2], Jinoh Lee[1,3]

***Abstract*— Impact robustness is critical when selecting and designing quasi-direct-drive (QDD) actuators for legged robots, yet currently used gear ratios vary widely. We derive a soft gear-ratio boundary beyond which reducing reflected inertia provides rapidly diminishing benefits for impact robustness. The boundary follows from factoring impact robustness into an energy-ratio term and an inertia-ratio term, with the latter exhibiting strong nonlinear behavior. Applying the resulting criterion to existing robots shows that proprioceptive designs with low collision energy can slightly exceed this boundary, whereas systems with larger link inertia remain below it. To support practical actuator selection, we also provide a browser-based calculator for real-time visualization of impact robustness across a wide parameter range. Together, these contributions enable rapid design exploration and provide a quantitative criterion for actuator selection in impact-prone legged robots.**

I. Introduction

In legged locomotion and fast manipulation tasks, weight-optimized robots frequently experience high-frequency impacts and sudden disturbances [1]. The corresponding actuation system must therefore provide both high dynamic performance and mechanical robustness under impact. One approach that combines lightweight joint designs [2] with collision tolerance is the use of an explicit mechanical spring in the drivetrain, as in series elastic actuators (SEAs) [3], where the elasticities beneficial effect on collision tolerance has been experimentally validated [4]. Furthermore, direct calculation of the stiffness required to achieve a given impact robustness enables fast design iterations [5]. However, the inherent compliance of the spring limits the force-control bandwidth [6], and the spring mass remains an optimization challenge [7].

An alternative to SEAs is to reduce reflected motor inertia in view of its negative influence on impact robustness [3] across actuator configurations [8]. This approach was pioneered as proprioceptive actuation, which combines high-torque motors with gear ratios as low as 5.8 and lightweight links, thereby enabling high transparency and high-bandwidth torque control [9]. The low gear ratio preserves many of the key benefits of direct-drive actuation [10]. The architecture became widely known as quasi-direct drive (QDD); however, early definitions based on single-stage planetary gearbox actuators (e.g., [11]) do not capture the broad range of gear ratios observed in commercially available QDDs that have recently emerged in the market as shown in Tab. I, Sec. III. In [12], the design rationale is supported by the Impact Mitigation Factor (IMF), which quantifies the reduction in Cartesian impact forces due to the projected inertias of motor and joint to the collision point. While useful for comparing system-level impact responses, the IMF does not directly relate to joint-level forces or provide insight into the mechanical limits of the drivetrain. Subsequent platforms leveraged high-torque, large-diameter motors to achieve direct-drive-like characteristics in humanoid systems [13]. More recently, commercial humanoids have adopted gear ratios exceeding 20 [14]. Such high gear ratios may undermine the benefits of QDD actuation because rotor-side dynamics, including inertia and friction, scale quadratically with the gear ratio N. Since the limited previously published experimental results could be explained without friction [15], [16], this work focuses on the influence of inertia, where the rotor inertia I_m is felt at the gearbox output as reflected motor inertia, or armature inertia, $I_\mathrm{a} = I_\mathrm{m}N^2$.

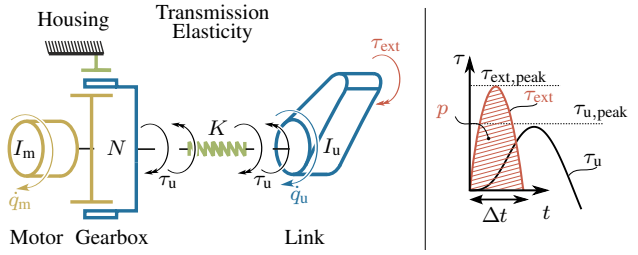


Fig. 1. Schematic diagram of the actuator model. The link inertia is connected to an ideal gearbox and rotor via a transmission elasticity K. An impulse p with sinusoidal torque profile on the external torque τ_ext and contact time Δt excites an oscillation of the gearbox interface torque τ_u defined at the gearbox output.

In this paper, impact robustness is given by the ratio of the maximum admissible joint impulse before exceeding the gearbox-interface torque limit and a reference impulse determined by the intended use case. We then address the question of which gear ratio provides the best trade-off between reflected inertia and output torque, while introducing a formalized criterion for impact robustness applicable to quasi-direct-drive actuators. Accordingly, this paper makes two main contributions:

- it factors the impact robustness equation, rooted in short-term contact mechanics of SEAs into an energy ratio term

This work was partly supported by the Council of Science & Technology (NST) grant by the Korea government No. GTL25041-000.

[1]German Aerospace Center (DLR), Institute of Robotics and Mechatronics, Germany, [2]Robotic Systems Lab, ETH Zurich, Switzerland, [3]KAIST, South Korea.

Corresponding author: anton.shu@dlr.de

This article is published by IEEE with Digital Object Identifier (DOI): XYZ-XXXXXXXXXXXX

© 2026 IEEE. Personal use of this material is permitted. Permission from IEEE must be obtained for all other uses, in any current or future media, including reprinting/republishing this material for advertising or promotional purposes, creating new collective works, for resale or redistribution to servers or lists, or reuse of any copyrighted component of this work in other works.

and an inertia ratio term. We show that the high nonlinearity of the latter enables the derivation of an analytical expression for a theoretical gear ratio limit beyond which the inertia term's positive influence on impact robustness erodes; and
- it introduces a practical browser-based calculator that enables real-time computation and visualization of impact robustness across a range of design parameters, supporting rapid design exploration.

II. Analysis of Impact Robustness

This section first derives the maximum gearbox-interface torque $\tau_{\mathrm{u,peak}}$ for a given transmitted impulse, then presents a physical interpretation based on a dimensionless reformulation, and concludes with two use cases.

A. Gearbox Interface Torque τ_u

Impact-induced gearbox-interface torque τ_{u} limits the lifetime of the gearbox and other actuator components. Fig. 1 shows the assumed two Degree-of-Freedom (DoF) actuator model with rotor inertia I_{m}, rotor velocity $\dot{q}_{\mathrm{m}}$, link inertia I_{u} and link velocity $\dot{q}_{\mathrm{u}}$. A gearbox with reduction ratio N transforms I_{m} at the gearbox output to the reflected motor inertia, or armature inertia, $I_{\mathrm{a}} = N^2 I_{\mathrm{m}}$. Structural elasticities of the gearbox and robot are modeled with a single concentrated stiffness K. Impacts result in a momentum exchange with impulse p, during which the external link torque τ_{ext} increases over a contact time Δt. We model this as a half-sine profile using the Heaviside function $H(t)$ as follows [16]:

$$\tau_{\mathrm{ext}}(t) = \sin\left(\frac{\pi t}{\Delta t}\right)\frac{\pi}{2\Delta t}(1 - H(t-\Delta t))p. \tag{1}$$

With (1), the governing equations of motion are given as

$$I_{\mathrm{m}}\ddot{q}_{\mathrm{m}} = N^{-1}\tau_{\mathrm{u}}, \tag{2}$$

$$K(q_{\mathrm{u}} - Nq_{\mathrm{m}}) = \tau_{\mathrm{u}}, \tag{3}$$

$$I_{\mathrm{u}}\ddot{q}_{\mathrm{u}} = -\tau_{\mathrm{u}} + \tau_{\mathrm{ext}}, \tag{4}$$

which are solved for τ_{u} using the Laplace transform with the Laplace variable s, similar to [5], as follows:

$$\tau_{\mathrm{u}}(t) = \mathcal{L}^{-1}\left(\frac{KI_{\mathrm{a}}}{I_{\mathrm{u}}I_{\mathrm{a}}s^2 + KI_{\mathrm{a}} + KI_{\mathrm{u}}}\mathcal{L}(p)\right), \tag{5}$$

$$= \begin{cases} \dfrac{Kp}{2I_{\mathrm{u}}\omega}\dfrac{a\sin\left(\frac{\omega}{a}t\right) - \sin(\omega t)}{1-a^2} & ,0 < t < \Delta t \\ \dfrac{Kp}{2I_{\mathrm{u}}\omega}\dfrac{\sin(\pi a - \omega t) - \sin(\omega t)}{1-a^2} & ,t \geq \Delta t \end{cases},$$

where $\omega = \sqrt{\left(\frac{K}{N^2 I_{\mathrm{m}}} + \frac{K}{I_{\mathrm{u}}}\right)}$ denotes the eigenfrequency, and $a = \frac{\Delta t\omega}{\pi}$ denotes the period factor that relates Δt to half of the period of the system $T_{1/2} = \frac{\pi}{\omega}$. Fig. 2 illustrates two cases of (5) with $\Delta t \leq T_{1/2}$ and $\Delta t > T_{1/2}$.

For $a < 1$, the system response with $t > 0$ is dominant and the peak gearbox-interface torque $\tau_{\mathrm{u,peak}}$ is derived following [16] as

$$\tau_{\mathrm{u,peak},\Delta t} = \frac{Kp}{I_{\mathrm{u}}\omega}\frac{\pi^2\cos\left(\frac{\Delta t\omega}{2}\right)}{\pi^2 - (\Delta t\omega)^2} \quad ,0 < \Delta t < \frac{\pi}{\omega}, \tag{6}$$

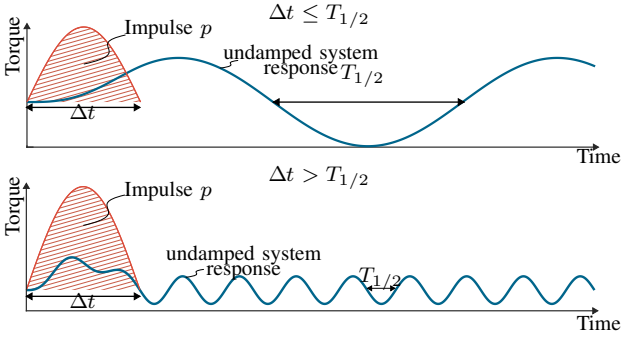


Fig. 2. Not-to-scale illustration of (5) for both short contact times $\Delta t \leq T_{1/2}$ and long contact times $\Delta t > T_{1/2}$. In both cases the impact excites a torque oscillation. For short contact times, only the first half period is disturbed, while for long contact times the system roughly follows the impact torque profile during the contact.

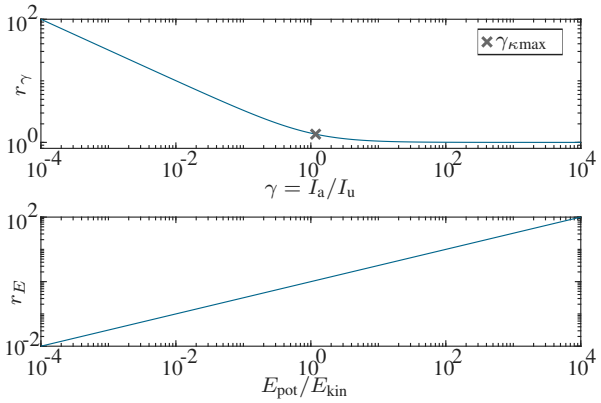


Fig. 3. Factors of the impact robustness r; energy-ratio term r_{E} and inertia-ratio term r_γ on a log-log plot with base $\beta = 10$. With respect to Motor-Link inertia ratio γ, the maximum-curvature point $\gamma_{\kappa\max}$ indicates a soft transition between two regions of influence.

which decreases monotonically as Δt increases within the following bounds:

$$\tau_{\mathrm{u,peak},0} = \lim_{\Delta t\to 0}\left(\tau_{\mathrm{u,peak},\Delta t}\right) = \frac{K}{I_{\mathrm{u}}\omega}p, \tag{7}$$

$$\tau_{\mathrm{u,peak},T_{1/2}} = \lim_{\Delta t\to \pi/\omega}\left(\tau_{\mathrm{u,peak},\Delta t}\right) = \frac{K}{I_{\mathrm{u}}\omega}\frac{\pi}{4}p. \tag{8}$$

Our analysis assumes concentrated linear elasticity that summarizes transmission and structural elasticities, negligible friction during the impact event, and no significant closed-loop control interactions over the contact interval. These assumptions are most appropriate for short contact-time impacts or short-term contacts with $\Delta t \leq T_{1/2}$. For such short-term contacts (5) has been experimentally verified [16]. For long-term contacts, (5) should therefore be interpreted as a theoretical approximation. When the impact disturbance becomes slower, interaction with closed-loop control becomes more likely, and the influence of friction remains unstudied in this contact-time domain.

B. Normalized Impact Robustness

We define an impact-robustness measure r as the ratio of the maximum admissible impact $p_{\max}$ to the reference

impact p_{ref}, i.e., $r = p_{\max}/p_{\text{ref}}$, for the worst-case contact-time $\Delta t \to 0$. With a maximum admissible torque at the gearbox interface $\tau_{\max}$ and (7) r becomes

$$r = \frac{p_{\max}}{p_{\text{ref}}} = \sqrt{\frac{I_{\text{u}}\tau_{\max}^2}{K p_{\text{ref}}^2}}\sqrt{\frac{I_{\text{a}} + I_{\text{u}}}{I_{\text{a}}}}. \tag{9}$$

Substitution of kinetic energy of the reference impulse $E_{\text{kin}} = \frac{1}{2}p_{\text{ref}}^2/I_{\text{u}}$, maximum potential energy of the drivetrain elasticities $E_{\text{pot}} = \frac{1}{2}\tau_{\max}^2/K$ and motor-link inertia ratio $\gamma = I_{\text{a}}/I_{\text{u}}$ yields

$$r(\gamma) = \underbrace{\sqrt{\frac{E_{\text{pot}}}{E_{\text{kin}}}}}_{r_E}\underbrace{\sqrt{\frac{\gamma+1}{\gamma}}}_{r_\gamma}. \tag{10}$$

Equation (10) reveals that impact robustness has two main factors. First, the energy-ratio term $r_E = \sqrt{E_{\text{pot}}/E_{\text{kin}}}$ and second the inertia-ratio term $r_\gamma = \sqrt{(\gamma+1)/\gamma}$. Fig. 3 shows both r_E and r_γ in a log-log plot. For r_E, a constant slope of $\frac{1}{2}$ is visible, while for r_γ the curvature $\kappa_{\hat{r}}(\delta)$ changes. Plotting the robustness reveals a transition region beyond which reductions in reflected inertia provide rapidly diminishing improvements in robustness. In the log-log plot it is defined over the logarithmic robustness $\hat{r}(\delta) = \log_\beta(r(\beta^\delta))$ with base β and transformed abscissa $\delta = \log_\beta(\gamma)$ as

$$\kappa_{\hat{r}}(\delta) = \left(\frac{\partial^2 \hat{r}(\delta)}{\partial \delta^2}\right) \Big/ \left(1 + \left(\frac{\partial \hat{r}(\delta)}{\partial \delta}\right)^2\right)^{3/2}, \tag{11}$$

with

$$\hat{r}(\delta) = \frac{1}{2\ln(\beta)}\left(\ln\left(\frac{E_{\text{pot}}}{E_{\text{kin}}}\right) + \ln\left(\frac{\beta^\delta + 1}{\beta^\delta}\right)\right). \tag{12}$$

In the parameter range $\delta \in \mathbb{R}$ or $\gamma \in \mathbb{R}^+$ a single extreme value for $\kappa_{\hat{r}}$ exists as $\gamma_{\kappa\max}$:

$$\begin{aligned}\gamma_{\kappa\max} &= \beta^{\left\{\arg\left(\partial\kappa_{\hat{r}}/\partial\delta=0\right)\middle|\,\delta\in\mathbb{R}\right\}} \\ &= \frac{\sqrt{22}}{3}\cos\left(\frac{1}{3}\arctan\left(\frac{3\sqrt{591}}{73}\right)\right) - \frac{1}{3} \\ &\approx 1.18.\end{aligned} \tag{13}$$

The varying curvature in the log-log plot $\kappa_{\hat{r}}$ highlights a highly nonlinear influence of γ on r. For values $\gamma \ll \gamma_{\kappa\max}$, a change in γ strongly influences r; for values $\gamma \gg \gamma_{\kappa\max}$, this influence becomes small. Note that $\gamma_{\kappa\max}$ is independent of E_{kin}, E_{pot} or β. We therefore interpret $\gamma_{\kappa\max}$ as a soft transition rather than a strict threshold and propose the following classification:

- $\gamma \lessapprox \gamma_{\kappa\max}$: QDD-like actuator.
  Changes in γ strongly influence impact robustness; reducing reflected inertia is therefore expected to be an effective design lever.
- $\gamma \gg \gamma_{\kappa\max}$: High-Inertia Actuator (HIA).
  Changes in γ have only a minor influence on impact robustness; therefore, robustness is expected to depend more heavily on other mechanisms such as elasticity, damping, structural strength, or reduced collision energy.

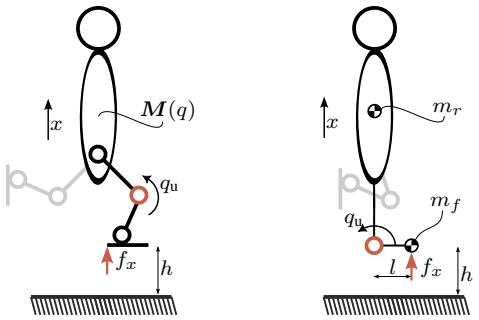


Fig. 4. Vertical drop-height configuration. **Left:** general case in which dropping a robot from height h with mass matrix $\boldsymbol{M}(\boldsymbol{q})$ creates a collision force f_x that is mapped to the joints via a Jacobian $\boldsymbol{J}_x^T$. **Right:** simplified case in which the mass of the foot is concentrated at the collision point and the collision force is mapped via l to the joint q_{u}.

With this classification, a gear-ratio limit can be computed for each actuator use case in which both I_{m} and I_{u} are known:

$$N_{\kappa\max} = \sqrt{\gamma_{\kappa\max}\frac{I_{\text{u}}}{I_{\text{m}}}}. \tag{14}$$

This analysis is based on the worst-case assumption of $\Delta t \to 0$. Increased values of Δt slightly shift the maximum-curvature point, which is acceptable because the proposed boundary is intended as a soft design indicator.

Traditional approaches to impact-robust actuators have focused on increasing E_{pot} by integrating dedicated springs [3]. A second approach is to minimize the reflected inertia I_{a} [11], hence reducing γ. A third approach is to reduce the reference kinetic energy E_{kin}, e.g. by reducing I_{u}. In the design of proprioceptive actuation, both I_{a} and I_{u} are minimized [9], [12].

Regarding the capacity for total collision torque $\tau_{\max}$ of the actuator, (10) reveals that, while $\tau_{\max}$ has a quadratic influence, the robustness r is governed by the total potential energy the actuator can absorb E_{pot}. A potential pitfall in the optimization of $\tau_{\max}$ is a simultaneous increase in K, which could decrease E_{pot} and thus reduce the total impact robustness r.

Equation (14) provides a criterion for selecting N. There is no universal gear ratio that makes an actuator QDD-like in terms of impact robustness. Instead, this classification depends on the rotor inertia I_{m} and attached link inertia I_{u} which is a use-case parameter. Thus, QDD-like impact robustness can be maintained for fixed I_{u} when a higher gear ratio N is compensated by a decrease of I_{m}.

C. Exemplary Reference Impact

This section discusses the considered reference impact cases, defined by the maximum link velocity and maximum drop height. These reference impacts are crucial for determining the kinetic energy E_{kin} used in the robustness equations above.

1) Maximum Link Velocity: A link moving around a stationary axis at maximum angular velocity $\dot{q}_{\text{max}}$ is stopped by an impulse $p_{\text{ref},\dot{q}}$, which changes the link energy by $E_{\text{kin},\dot{q}}$. Both values then follow as

$$p_{\text{ref},\dot{q}} = -I_{\text{u}}\dot{q}_{\text{max}}, \tag{15}$$

$$E_{\text{kin},\dot{q}} = \frac{1}{2} I_{\text{u}} \dot{q}_{\text{max}}^2. \tag{16}$$

2) Maximum Drop Height: A robot visualized on the left of Fig. 4 with n minimal coordinates $\boldsymbol{q}$, rigid-body mass matrix $\boldsymbol{M}(\boldsymbol{q})$, and no initial joint velocities is dropped from a height h_{ref} along Cartesian coordinate x, where ground acceleration g is present. The robot impacts the ground with a relative velocity $\Delta v = \sqrt{2gh_{\text{ref}}}$ and a contact normal along x. For this short-term prediction we assume that the joint configuration $\boldsymbol{q}$ does not change during Δt. The force f_x experienced by the contact point during impact is transformed to $\boldsymbol{q}$ with a Jacobian $\boldsymbol{J}_x(\boldsymbol{q})$ as $\boldsymbol{\tau}_{\text{ext}} = \boldsymbol{J}_x^T f_x$. The scalar collision inertia λ_x is then given as

$$\lambda_x(\boldsymbol{q}) = \left(\boldsymbol{J}_x \boldsymbol{M}^{-1} \boldsymbol{J}_x^T \right)^{-1}. \tag{17}$$

The impulse experienced by the joints is therefore $\boldsymbol{p}_{\text{ref},h}$, from which the total kinetic energy released in the system, $E_{\text{kin},h,tot}$, follows as

$$\boldsymbol{p}_{\text{ref},h} = \boldsymbol{J}_x^T \lambda_x \sqrt{2gh_{\text{ref}}}, \tag{18}$$

$$\begin{aligned} E_{\text{kin},h,tot} &= \frac{1}{2} (\boldsymbol{J}_x^T \lambda_x)^T \boldsymbol{M}^{-1} \boldsymbol{J}_x^T \lambda_x \left(2gh_{\text{ref}}\right), \\ &= \lambda_x g h_{\text{ref}}. \end{aligned} \tag{19}$$

The link coordinate of interest is the i-th element of $\boldsymbol{q}$ which we extract with the unit vector $\boldsymbol{e}_i$ as $q_{\text{u}} = \boldsymbol{e}_i \boldsymbol{q}$. With this, $\tau_{\text{ext}} = \boldsymbol{e}_i \boldsymbol{J}_x^T f_x$ and it follows

$$p_{\text{ref},h} = \boldsymbol{e}_i \boldsymbol{J}_x^T \lambda_x \sqrt{2gh_{\text{ref}}}. \tag{20}$$

In this case, I_{u} is the apparent inertia associated with a Cartesian impulse p_x that creates a joint-velocity change $\Delta\dot{q}_{\text{u}}$ as

$$\begin{aligned} I_{\text{u}} \Delta\dot{q}_{\text{u}} &= \boldsymbol{e}_i \boldsymbol{J}_x^T p_x, \\ I_{\text{u}} \boldsymbol{e}_i \boldsymbol{M}^{-1} \boldsymbol{J}_x^T p_x &= \boldsymbol{e}_i \boldsymbol{J}_x^T p_x, \\ I_{\text{u}} &= \frac{\boldsymbol{e}_i \boldsymbol{J}_x^T}{\boldsymbol{e}_i \boldsymbol{M}^{-1} \boldsymbol{J}_x^T}. \end{aligned} \tag{21}$$

From this, the kinetic energy released by the impact in joint i is derived as follows:

$$E_{\text{kin},h} = \underbrace{\frac{\left(\boldsymbol{e}_i \boldsymbol{J}_x^T\right)^2 \lambda_x}{I_{\text{u}}}}_{f_i} \lambda_x g h_{\text{ref}}, \tag{22}$$

where f_i is the factor of absorbed energy in joint i as $f_i = E_{\text{kin},h}/E_{\text{kin},h,tot}$. For a worst-case approximation we propose to use $f_i = 1$.

In the simplified case shown on the right of Fig. 4, the foot joint j and the collision point are aligned horizontally and separated by l such that $\boldsymbol{J}_x^T = \boldsymbol{e}_j \left| \boldsymbol{J}_x^T \right| = \boldsymbol{e}_j l$. Additionally all mass in the foot m_f is concentrated in the collision point. In this case $I_{\text{u},s} = m_f l^2$ and hence $f_i = 1$. We can therefore give a simplified expression for the corresponding impulse $p_{\text{ref},h,s}$ on the foot joint q_{u}, with the reference kinetic-energy change $E_{\text{kin},h,s}$

$$p_{\text{ref},h,s} = l m_f \sqrt{2gh_{\text{ref}}}, \tag{23}$$

$$E_{\text{kin},h,s} = m_f g h_{\text{ref}}. \tag{24}$$

This result may initially appear counterintuitive: the apparent inertia must be used for I_{u}, and this inertia depends on both the robot configuration and the contact location. For example, an impact directly below the ankle joint creates no torque load on the joint, but it does create structural loads in its bearings. We therefore recommend including structural loads as constraints when optimizing I_{u}.

3) Contact Time Estimation: A worst-case contact time Δt can be estimated from the contact stiffness c and the assumption of a single-DoF spring-mass collision model [5] as

$$\Delta t = \pi \sqrt{\lambda_x / c} \tag{25}$$

Structural elasticities of the links between impact and joint are likely to increase Δt experienced at the joint. Therefore, these elasticities should be respected in c or K.

D. Relation to Impact Mitigation Factor

Both the IMF defined by Wensing et al. [12] and (9) relate the reflected motor inertia to the inertia of the rest of the system. The difference between the two metrics is that the IMF computes a measure of the total impulse experienced during an impact by combining the effects of reflected and link inertia, whereas for r, the impulse following an impact on the rigid body, neglecting reflected inertia, is projected to a single joint. At the single joint, r compares the joint torque with the maximum admissible gearbox-interface torque τ_{max}. To do so, r relates rotational inertia through r_γ and accounts for the inertia projected to the collision point Λ via E_{kin} in r_E. The IMF assumes that I_{a} influences the collision forces, while for r we assume that transmission elasticities decouple I_{a} from the impact event. The latter assumption is justified for short-contact-time impacts. In summary, both measures are valuable tools to cover different aspects of the system design.

III. Interactive Calculator

The previous section focused on the general influence of parameters on the design space. For a specific design, the underlying equations must be evaluated at the corresponding design point. Furthermore, parameter exploration helps build design intuition. This section therefore introduces an interactive browser-based calculator for real-time computation and visualization of impact robustness, shown in Fig. 5, which can be accessed at `https://github.com/DLR-RM/drop-height-calculator`.

Our calculator is based on the assumption that the user wants to explore impact robustness for a use case such as a

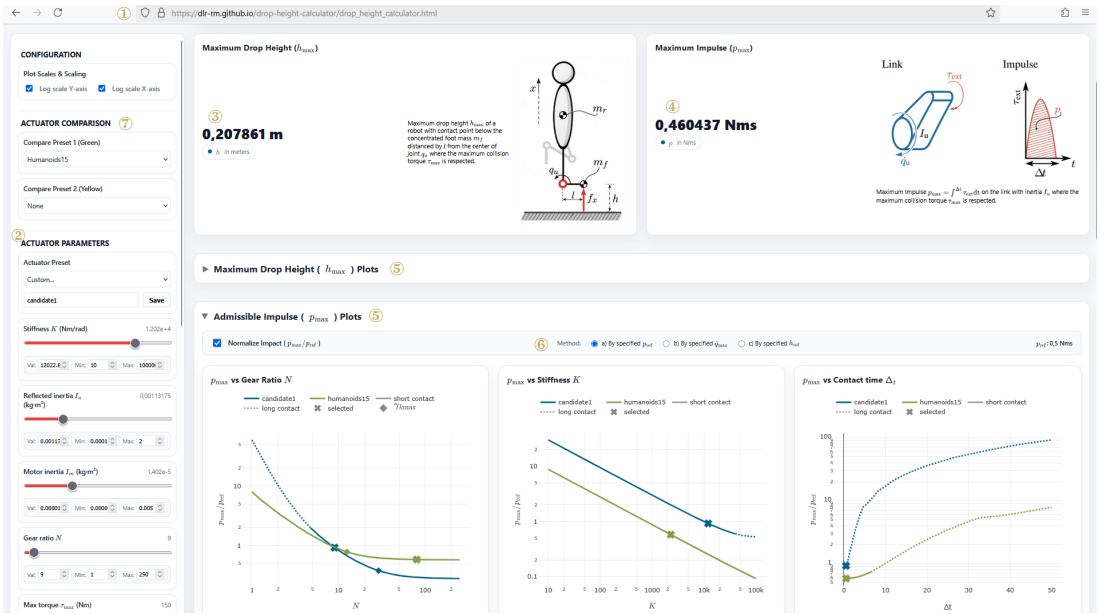


Fig. 5. Screenshot of the interactive impact-robustness calculator. The interface allows users to vary actuator and use-case parameters, compare saved actuator presets, and visualize maximum admissible impact and drop height in real time.

sudden stop at maximum link velocity or a maximum drop height. A set of parameters that represent a candidate actuator can be varied by sliders. As a result, the robustness metrics of maximum admissible impact $p_{\max}$ and maximum drop height $h_{\max}$ are calculated together with several plots that show parameter sensitivity at the current design point. The user can save parameter sets for both candidate actuators and candidate use cases during a session to keep track of the design point. Furthermore, up to two saved actuator presets can additionally be displayed in the interactive plots.

The plots highlight the selected design point for each actuator preset, as well as the parameter values that correspond to $\gamma_{\kappa\max}$ similar to (14) if applicable. A change of maximum and minimum parameter values will change both the range of the sliders and the x-axis limits of the plots. For small parameter ranges, we recommend disabling the log-log view for each axis. The plots distinguish between short-term contacts $\Delta t \leq T_{1/2}$ using (6) and long-term contacts with $\Delta t > T_{1/2}$ using numerical maximum search. Here, our calculator shows some local maxima of r which we attribute to frequency matching effects when $\Delta t = zT_{1/2}, z \in \mathbb{Z}^+$. The unmodeled friction will influence both the natural frequency and $T_{1/2}$ as well as the total torque response of the system. We recommend avoiding design optimization based on these local maxima and validating the actuator choice when $\Delta t > T_{1/2}$ with a numerical simulation that includes friction and closed-loop control. When $\Delta t \gg T_{1/2}$, the sometimes drastic increase in r points to a potentially counterintuitive optimization. Theoretically, closed-loop impact mitigation could be achieved by designing a system with high transmission stiffness, yielding a very small $T_{1/2}$, alongside low contact stiffness, yielding a low Δt. The drawback to this approach is that it requires highly reliable control systems and contradicts conventional safety approaches in which the system is switched off upon failure.

We identified two actuators in [15] and [16], respectively, for which all required parameters are disclosed, and we added them as preconfigured presets in our calculator. Note that we have not included commercially available actuators in the presets since not all parameters are disclosed. Tab. I lists the actuators for which we could identify at least two of the following parameters: N, I_{m} and $\tau_{\max}$; however, because no value of K is disclosed, it is omitted from the table.

TABLE I
COMMERCIALLY AVAILABLE ACTUATORS

	Gear ratio N	Reflected inertia I_{a} [kg m^2]	Peak delivered torque [Nm]	Peak collision torque $\tau_{\max}$ [Nm]
CubeMars				
AKE90-8 [17]	8	2.1×10^{-2}	170	–
AKH70-48 [18]	48	1.2×10^{-1}	222	–
MyActuator				
RMD-X8-P20 [19]	19.6	5.8×10^{-2}	120	–
RMD-X12-P20 [20]	20	1.3×10^{-1}	320	–
Westwood Robotics				
Mountain BEAR [21]	14.1	7.2×10^{-2}	155	–
Kodiak BEAR [21]	7.7	1.2×10^{-1}	350	–
Maxon				
HEJ-90 [22]	–	4.5×10^{-2}	140	320
Synapticon				
Actilink-JD12 [23]	9	4×10^{-2}	120	–
Actilink-DUO [24]	20	3.3×10^{-1}	200	–

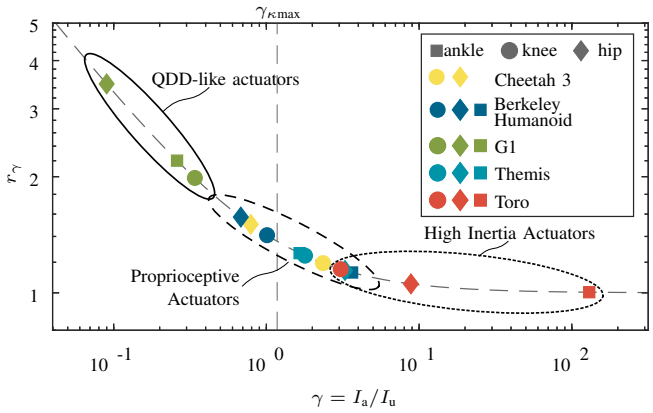


Fig. 6. Inertia-Ratio contribution to impact robustness r_γ over Motor-Link Inertia Ratio γ in a log-log plot with values of different legged-locomotion systems listed in Tab. II.

IV. Application to Existing Robots

This section applies our proposed soft classification of QDD from Sec. II-B to existing robotic systems. To do so, it compares the inertia ratios γ and impact inertia λ_x of robotic systems for which these values can be computed from disclosed data, as shown in Tab. II and Fig. 6, for one specific impact pose.

We selected legged robotic systems with a total mass exceeding 15 kg that have publicly disclosed actuator reflected inertia I_a and rigid-body mass models. We define a leg pose similar to the left of Fig. 4 with a slightly collapsed leg, the foot between hip and knee, and a vertical-impact contact point at the back of the heel, because several running videos show a similar ground-contact configuration [25]–[27]. Using this pose we compute impact inertia λ_x and apparent link inertia I_u together with the inertia ratio γ for each joint. The exact pose used for each system is defined in Tab. II which shows the result of the computation together with Fig. 6. Our comparison reveals that DLR Toro exhibits very high γ values paired with a high λ_x value. The expected low robustness is consistent with its usual restrictive operation on a safety crane and the actuators can be classified as HIA. The other, much more recent systems have much lower inertia ratios, in line with their more permissive operation. The MIT Cheetah 3, Berkeley Humanoid, and Westwood Robotics Themis robots show slightly higher $\gamma > \gamma_{\kappa\max}$ values, especially for their ankle pitch joints in our configuration. We hypothesize that, in these cases, a low value of r_E guarantees robustness, e.g., due to transmission elasticities or relatively low total contact inertia λ_x. The latter is an explicit design goal for Cheetah 3 [28] and Themis predecessor Artemis [13], in line with the definition of proprioceptive actuation [12]. In comparison, the Unitree G1 exhibits higher values of λ_x but very low $\gamma < \gamma_{\kappa\max}$, likely relying on r_γ for impact robustness consistent with our QDD-like actuator classification.

TABLE II
Inertia Ratio in Leg Pitch Joints of Existing Robots

System	N [-]	I_a [kgm^2]	I_u [kgm^2]	q_u [rad]	γ [-]	λ_x [kg]
MIT Cheetah 3 [28], [29]						
knee	8.82	6.8e-2	3.0e-2	0.78	**2.28**	1.5
hip	7.76	6.0e-2	7.6e-2	-1.17	**0.79**	1.5
Berkeley Humanoid [30], [31]						
ankle	9	5.6e-3	1.5e-3	-0.3	**3.64**	0.9
knee	9	1.2e-2	1.2e-2	1.17	**1.01**	0.9
hip	9	7.6e-3	1.1e-2	0.78	**0.68**	0.9
Westwood Robotics Themis [21], [32]						
ankle	20	9.e-3	5.4e-3	0.39	**1.65**	0.9
knee	7.7	1.2e-1	6.4e-2	-1.17	**1.79**	0.9
hip	7.7	1.2e-1	3.5e-2	0.78	**3.27**	0.9
Unitree G1 [14], [33]						
ankle	16	7.2e-3	1.4e-2	-0.39	**0.52**	3.0
knee	22.5	2.5e-2	7.4e-2	1.17	**0.34**	3.0
hip	14.3	1.0e-2	1.1e0	-0.78	**0.09**	3.0
DLR Toro [34]						
ankle	100	1.7e0	1.3e-2	-0.39	**130**	8.1
knee	100	1.7e0	5.4e-1	1.17	**3.07**	8.1
hip	160	2.2e0	2.5e-1	-0.78	**8.84**	8.1

V. Conclusion

This paper analyzes the impact robustness of quasi-direct-drive actuators by reformulating the peak gearbox-interface torque as a normalized robustness measure composed of an energy-ratio term and an inertia-ratio term. The resulting formulation reveals a strongly nonlinear dependence on the motor-link inertia ratio γ, with a characteristic curvature maximum at $\gamma_{\kappa\max} \approx 1.18$. This value provides a soft boundary between QDD-like actuators, for which changes in reflected motor inertia strongly affect impact robustness, and high-inertia actuators, for which robustness must rely mainly on other mitigation mechanisms. The resulting criterion shows that there is no universal gear-ratio limit for QDD-like actuators with regards to impact robustness. Instead, the relevant boundary depends on the ratio between reflected motor inertia and the apparent link inertia of the specific use case. This makes $\gamma_{\kappa\max}$ a practical design indicator: below or near this value, reducing reflected motor inertia remains highly effective, whereas far above it, designers should expect diminishing returns and rely on additional robustness mechanisms. We applied our method to existing robot systems and found that conventional systems with limited impact tolerance exceed $\gamma_{\kappa\max}$, while systems with strongly optimized link mass and therefore reduced collision energy only slightly exceed $\gamma_{\kappa\max}$. Finally, we identified a representative system with higher link mass for which $\gamma < \gamma_{\kappa\max}$. We further introduced an interactive browser-based calculator to support real-time exploration of actuator and use-case parameters. Together, these contributions have the

potential to massively improve actuator selection in impact-prone robotic systems, particularly dynamic legged robots.

REFERENCES

[1] K. Fründ, F. Beck, A. Shu, F. Loeffl, and J. Lee, "Bipedal running: Bioinspired fundamentals for versatile humanoid robot locomotion," in *Proc. IEEE/RAS International Conference on Humanoid Robots*, 2023, pp. 1–8.

[2] G. Hirzinger, A. Albu-Schaffer, M. Hahnle, I. Schaefer, and N. Sporer, "On a new generation of torque controlled light-weight robots," in *Proc. IEEE International Conference on Robotics and Automation*, vol. 4, 2001, pp. 3356–3363 vol.4.

[3] G. Pratt and M. Williamson, "Series elastic actuators," in *Proc. IEEE/RSJ International Conference on Intelligent Robots and Systems*, vol. 1, 1995, pp. 399–406.

[4] S. Haddadin, T. Laue, U. Frese, S. Wolf, A. Albu-Schäffer, and G. Hirzinger, "Kick it with elasticity: Safety and performance in human–robot soccer," *Robotics and Autonomous Systems*, vol. 57, no. 8, pp. 761–775, 2009.

[5] A. Shu, C. Raschel, M. Keppler, A. Wedler, and M. Görner, "Impact Robustness Versus Torque Bandwidth: A Design Guide for Differential Elastic Actuators," *IEEE Transactions on Robotics*, vol. 40, pp. 3657–3675, 2024.

[6] W. Townsend and J. Salisbury, "Mechanical bandwidth as a guideline to high-performance manipulator design," in *Proc. IEEE International Conference on Robotics and Automation*, vol. 3, 1989, pp. 1390–1395.

[7] Z. Bons, G. C. Thomas, L. Mooney, and E. J. Rouse, "An Energy-Dense Two-Part Torsion Spring Architecture and Design Tool," *IEEE/ASME Transactions on Mechatronics*, pp. 1–12, 2023.

[8] M. Hutter, "StarlETH & Co.: Design and control of legged robots with compliant actuation," Ph.D. dissertation, ETH Zurich, 2013.

[9] S. Seok, A. Wang, D. Otten, and S. Kim, "Actuator design for high force proprioceptive control in fast legged locomotion," in *Proc. IEEE/RSJ International Conference on Intelligent Robots and Systems*, 2012, pp. 1970–1975.

[10] G. Kenneally, A. De, and D. E. Koditschek, "Design Principles for a Family of Direct-Drive Legged Robots," *IEEE Robotics and Automation Letters*, vol. 1, no. 2, pp. 900–907, Jul. 2016.

[11] S. Kalouche, "Design for 3D Agility and Virtual Compliance Using Proprioceptive Force Control in Dynamic Legged Robots," Ph.D. dissertation, Carnegie Mellon University, 2017.

[12] P. M. Wensing, A. Wang, S. Seok, D. Otten, J. Lang, and S. Kim, "Proprioceptive Actuator Design in the MIT Cheetah: Impact Mitigation and High-Bandwidth Physical Interaction for Dynamic Legged Robots," *IEEE Transactions on Robotics*, vol. 33, no. 3, pp. 509–522, 2017.

[13] T. Zhu, M. S. Ahn, and D. Hong, "Design and Experimental Study of BLDC Motor Immersion Cooling for Legged Robots," in *Proc. International Conference on Advanced Robotics*, Dec. 2021, pp. 1137–1143.

[14] A. Wang, "Unitree_rl_lab," Unitree Robotics, Oct. 2025, accessed: July 24, 2026. [Online]. Available: https://github.com/unitreerobotics/unitree_rl_lab/commit/945cb7b

[15] F. Negrello, M. Garabini, M. G. Catalano, J. Malzahn, D. G. Caldwell, A. Bicchi, and N. G. Tsagarakis, "A modular compliant actuator for emerging high performance and fall-resilient humanoids," in *Proc. IEEE/RAS International Conference on Humanoid Robots*, 2015, pp. 414–420.

[16] A. Shu, F. Loeffl, A. Kolb, K. Fründ, D. Wandinger, F. Beck, J. Reinecke, M. Grebenstein, M. Hutter, and J. Lee, "Maximum stiffness of impact-robust actuators in highly dynamic robotics tasks: Application to series elastic actuator design," *IEEE Robotics and Automation Letters*, vol. 11, no. 9, pp. 10 879–10 886, 2026.

[17] CubeMars. (2026) QDD AKE90-8 datasheet. Accessed: July 24, 2026. [Online]. Available: https://www.cubemars.com/images/file/20230703/1688352405877552.pdf

[18] CubeMars Documentation. (2026) QDD AKH70-48 datasheet. Accessed: July 24, 2026. [Online]. Available: https://www.cubemars.com/data/cms/202602/ak-series-prodcut-manual-v3-2-0-for-ak-3-0-robotic-actuator.pdf

[19] MyActuator. (2026) RMD-X8-P20-120-E Product Page. Accessed: July 24, 2026. [Online]. Available: https://www.myactuator.com/x8-120details

[20] ——. (2026) RMD-X12-P20-320-E Product Page. Accessed: July 24, 2026. [Online]. Available: https://www.myactuator.com/x12-320-details

[21] Westwood Robotics. (2026) BEAR Series Actuator Product Manual v 1.0.0. Accessed: July 24, 2026. [Online]. Available: https://www.westwoodrobotics.io/wp-content/uploads/2026/06/BEAR-Product-Manual-EN-V1.0.0.pdf

[22] maxon international ltd. (2026) HEJ 90-48-140 Datasheet. Accessed: July 24, 2026. [Online]. Available: https://global.maxongroup.com/hubfs/Datasheet_HEJ_90_48_140_rev2.3.pdf?hsLang=en

[23] Synapticon. (2026) ACTILINK-JD12 Documentation. Accessed: July 24, 2026. [Online]. Available: https://synapticon-documentation.s3.eu-west-1.amazonaws.com/ACTILINK-JD+Documentation.pdf

[24] ——. (2026) ACTILINK-DUO Documentation. Accessed: July 24, 2026. [Online]. Available: https://synapticon-documentation.s3.eu-west-1.amazonaws.com/actilink-jb-datasheet_20260610.pdf

[25] Boston Dynamics. (2025, Mar.) Walk, Run, Crawl, RL Fun | Boston Dynamics | Atlas. Accessed: July 24, 2026. [Online]. Available: https://www.youtube.com/watch?v=I44_zbEwz_w

[26] M. Milford. (2025, Jun.) Unitree G1 Humanoid Robot Running at USC Campus. Accessed: July 24, 2026. [Online]. Available: https://www.youtube.com/watch?v=6mtoF1ONL1c

[27] BBC News. (2025, Aug.) Robots race at World Humanoid Robot Games. Accessed: July 24, 2026. [Online]. Available: https://www.gettyimages.com/video/2231301971

[28] G. Bledt, M. J. Powell, B. Katz, J. Di Carlo, P. M. Wensing, and S. Kim, "MIT Cheetah 3: Design and Control of a Robust, Dynamic Quadruped Robot," in *Proc. IEEE/RSJ International Conference on Intelligent Robots and Systems*, 2018, pp. 2245–2252.

[29] MIT Biomimetic Robotics Lab, "Cheetah-software," MIT Biomimetic Robotics Lab, accessed: July 24, 2026. [Online]. Available: https://github.com/mit-biomimetics/Cheetah-Software

[30] Q. Liao, B. Zhang, X. Huang, X. Huang, Z. Li, and K. Sreenath, "Berkeley Humanoid: A research platform for learning-based control," in *Proc. IEEE International Conference on Robotics and Automation*, 2025, pp. 2897–2904.

[31] Q. Liao, "Berkeley Humanoid Robot Description (URDF)," HybridRobotics, accessed: July 24, 2026. [Online]. Available: https://github.com/HybridRobotics/berkeley_humanoid_description/commit/ab26a86

[32] X. Zhang, "THEMIS Models for Simulation," Westwood Robotics, 2025, accessed: July 24, 2026. [Online]. Available: https://github.com/Westwood-Robotics/THEMIS-Simulation-Model/commit/d3abb0a

[33] K. Zakka, Y. Tassa, and MuJoCo Menagerie Contributors, "MuJoCo Menagerie: A collection of high-quality simulation models for MuJoCo," 2022, accessed: July 24, 2026. [Online]. Available: http://github.com/google-deepmind/mujoco_menagerie

[34] J. Englsberger, A. Werner, C. Ott, B. Henze, M. A. Roa, G. Garofalo, R. Burger, A. Beyer, O. Eiberger, K. Schmid, and A. Albu-Schäffer, "Overview of the torque-controlled humanoid robot TORO," in *Proc. IEEE/RAS International Conference on Humanoid Robots*, Nov. 2014, pp. 916–923.